Transp Porous Med
DOI 10.1007/s11242-016-0757-0

An Analysis of Unsteady Flooding Processes: Varying Force Balance and the Applicability of Steady-State Upscaling

Sindre T. Hilden[1,2] · **Carl Fredrik Berg**[3]

Received: 12 June 2015 / Accepted: 9 August 2016

Abstract A widely used approach for upscaling relative permeability is based on a steady-state assumption. For small time intervals and at small scales, the flooding process can be approximated as being in a steady state. However, at large scales with large time steps, water flooding of a reservoir is an unsteady process. In this article, we first investigate the balance of viscous, capillary and gravity forces on the fine scale during the water flooding of a reservoir at different flow velocities. We introduce a semi-analytical method to find the low-rate limit solution, while the high-rate limit solution is found by running a simulation without gravity and capillary pressure. These limit solutions allow us to understand when rate-dependent simulations approach a point where some forces become negligible. We perform a series of numerical simulations on the fine scale to construct solution transitions between the established outer limits. Simulations are run both on homogeneous models, on different layered models and on a more complex two-dimensional model. The rate-dependent simulations show smooth transitions between the low- and high-rate limits, and these transitions are in general non-trivial. In all our example cases, one of the limit solutions gives a lower bound for the rate dependent results, while they do not in general provide an upper bound. Based on the rate-dependence of the force balance, we evaluate when different steady-state upscaling procedures are applicable for an unsteady flooding process. We observe that the capillary-limit upscaling, which also takes gravity into account, reproduces the low-rate limit fine-scale simulations. Such capillary-limit upscaling is also able to reproduce the transition to capillary equilibrium normal to the flow direction. As already known, the viscous-limit upscaling is only applicable when we have close to constant fractional flow within each coarse grid block.

✉ Sindre T. Hilden
sindre.t.hilden@gmail.com

Carl Fredrik Berg
carlpaatur@hotmail.com

[1] Department of Mathematics, NTNU, Trondheim, Norway

[2] Department of Applied Mathematics, SINTEF, P.O. Box 124, Blindern, 0314 Oslo, Norway

[3] Statoil R&D Center, Arkitekt Ebbels veg 10, Rotvoll, 7053 Trondheim, Norway

Published online: 16 August 2016

Keywords Steady-state upscaling · Relative permeability · Capillary limit · Viscous limit · Capillary number

1 Introduction

Two-phase incompressible flow through porous media at a macroscopic (Darcy) scale is governed by viscous, capillary and gravity forces (Bear 1988; Lake 1989; Rapoport 1955). The balance of these forces affects the flooding process of a reservoir, and there is thus a need for quantifying the relative influence of them.

Traditionally, the balance of these forces has been calculated from dimensionless equations, or scaling groups, including capillary and gravity numbers (Lake 1989; Rapoport 1955; Shook et al. 1992; Zhou et al. 1997). The capillary number characterizes the ratio of viscous to capillary forces, while the gravity number characterizes the ratio of gravitational to capillary forces. There exists a range of more of less equivalent forms of both the capillary and the gravity numbers. An overview of different capillary numbers can be found in e.g., Lake (1989, Table 3-2), and an overview of different gravity numbers can be found in e.g., Shook et al. (1992).

Deciding whether the flow is capillary, gravity or viscous dominated will depend upon which dimensionless numbers are used. Also, as the balance of forces varies temporarily in a reservoir, any single number cannot fully characterize the flow process. In Stephen et al. (2001), the two-phase transport equations were formulated with terms related to viscous, capillary and gravity forces. This enabled the visualization of the changing force balance between these three forces during a simulation, both in space and time.

Reservoirs are generally heterogeneous on different length scales (Aarnes et al. 2007; Kløv et al. 2003), and it can be important to capture the effect of small-scale heterogeneities to determine large-scale flooding processes (Kjonsvik et al. 1994). As length scales for heterogeneities might differ by several orders of magnitude, it is not always possible to represent them all in a single model. Upscaling of flow parameters is therefore necessary to include effects of smaller-scale heterogeneities into coarser-scale models.

There is a wide range of upscaling methods both for one-phase (Renard and Marsily 1997; Farmer 2002; Durlofsky 2003) and for two-phase flow (Barker and Thibeau 1997; Christie 2001; Durlofsky 2005). In the case of one-phase flow, the permeability (or transmissibility) is upscaled to represent the fine-scale flow on a coarser scale. For two-phase flow, the saturation dependency of the phase permeabilities needs to be accounted for, and the relative permeability curves must also be upscaled, possibly in addition to capillary pressure curves. Two of the main classes of upscaling procedures are averaging methods and flow-based methods. The latter is considered more accurate, however more computationally demanding. The flow-based methods can be further divided into global and local methods (Durlofsky 2005). For two-phase upscaling, global methods are typically applied to upscaling of viscous-dominated flow from a geocellular model to a simulation model (Kyte and Berry 1975; Zhang et al. 2006), while local methods are typically applied to determine effective flow properties for rock types or facies in geocellular models (Kløv et al. 2003; Rustad et al. 2008).

Steady-state upscaling is a local upscaling method for two-phase flow (Pickup et al. 2000; Smith 1991). Water flooding of a reservoir is a transient process, but the flooding process at a small scale, e.g., on the core scale, can still often be approximated as steady-state because the saturation changes are small relative to the volume of fluids flowing through the rock (Ekrann and Aasen 2000). With larger scales, the steady-state assumption becomes decreasingly valid. Steady-state upscaling is therefore mainly used on a relatively small scale, e.g., from a lamina scale (mm to cm) to a bed scale (cm to m) (Ringrose et al. 1993).

The main challenge for a multiphase steady-state upscaling is to determine the fine-scale saturation distribution, which is rate dependent. The limiting cases of the force balance are important for upscaling, as determining the saturation distribution can be greatly simplified in these limits (Ekrann and Aasen 2000). On small scales, i.e., from the pore scale and up to cell sizes of about a meter, it is common to assume that capillary forces dominate for typical reservoir flow rates (Dale et al. 1997). For very high flow rates, the viscous forces will dominate, and simplifications can again be made (Ekrann and Aasen 2000). For intermediate flow rates, simplifications are typically not possible, and one has to perform a flow simulation on each coarse grid block with some choice of boundary conditions until a steady state is reached. In special case of a one-dimensional model, an analytical solution was used in Dale et al. (1997) to compute the saturation distribution for intermediate flow velocities, between the limiting low- and high-rate cases.

Another challenge in steady-state upscaling is to validate the steady-state assumption. In Ekrann and Aasen (2000), the steady-state solutions of a two-dimensional medium were studied, and the validity of the steady-state limits was assessed depending on the boundary condition and the distance from the inlet. In Jonoud and Jackson (2008), using the inspectional analysis of Shook et al. (1992), the force balance between capillary and viscous forces was described using dimensionless groups. These groups were then used to determine the validity of either capillary- or viscous-limit steady-state upscaling for two-dimensional layered models. It was shows that three different scaling groups were required to describe the force balance, the end point mobility ratio and transverse and longitudinal Peclet numbers, for flow across and along layers, respectively. A capillary number that take the geometrical distribution of rock types into account was introduced in Odsæter et al. (2015) and used to determine the validity of capillary- or viscous-limit steady-state upscaling for complex three-dimensional models with a set of flow parameters.

The transition between capillary- and viscous-limit steady-state upscaling has been investigated for two-dimensional models in Lohne et al. (2006) and Virnovsky et al. (2004) and later extended to three-dimensional models in Odsæter et al. (2015). It was noted that the transition between the upscaled capillary- and viscous-limit flow parameters could be non-monotonic and not necessarily bounded by the limiting cases.

In this article, we will investigate the balance of forces by numerical simulations on the fine scale. We introduce a semi-analytical method for obtaining solutions of the flooding process for vanishing flow rates. Running numerical simulations dominated by capillary forces and gravity is computationally heavy, and this semi-analytical method allows us to easily establish a lower limit solution for the rate-dependent simulations. For the high-rate limit, solutions can be obtained by ignoring capillary pressure and gravity in the flow simulations. These cases serve as boundaries for the rate-dependent flow.

By considering how the solution changes with respect to the flow rate, and how it compares to the solution limits, we are able to judge when the limiting cases are valid simplifications. Moreover, we observe distinct rate ranges where forces dominate along or perpendicular to the flow direction and investigate the transition between these distinct rate regimes.

In addition to studying how different forces interact on the fine scale through a wide range of flow rates, we perform steady-state upscaling and assess for what flow rates and scales the upscaling is valid. We include gravity in addition to viscous and capillary forces, in contrast to e.g., Jonoud and Jackson (2008) and Virnovsky et al. (2004). The validity of the upscaling methods is explained in light of the fine-scale force balance. For the high-rate limit, it has been pointed out earlier that the viscous-limit upscaling method is appropriate for stable displacement provided separation of scales holds (Ekrann and Aasen 2000). The capillary-limit upscaling is typically valid for a wider range of models and flow rates, as will be discussed in this paper.

Upscaling, general calculations and plotting in this article are performed by the use of the MATLAB Reservoir Simulation Toolbox (MRST) (Lie et al. 2012; MATLAB 2015a), which is an open-source toolbox for rapid prototyping of new computational methods for reservoir engineering. The flow simulations are conducted using the fully implicit solver of the commercially available reservoir simulator Eclipse 100 (http://www.slb.com/eclipse/).

This article has the following outline: We state the governing flow equations in Sect. 2. Section 3 presents limiting solutions for the rate-dependent flooding process. In particular, we introduce a semi-analytical low-rate solution. Thereafter, we present different steady-state upscaling procedures in Sect. 4. In Sect. 5, we use simulations at different rates to investigate the force balance between viscous, capillary and gravitational forces. We investigate steady-state upscaling procedures for the different rate regimes in Sect. 6 to address when the different methods are applicable. To consider the force balance and upscaling in a general context, a more complex heterogeneous model is studied in Sect. 7. In Sect. 8, we summarize and discuss the results of this article.

2 Governing Equations

We consider incompressible two-phase flow. The two phases will be denoted oil and water, represented by subscripts o and w. The continuity equations for the two phases are

$$\phi \frac{\partial s_\alpha}{\partial t} + \nabla \cdot \mathbf{v}_\alpha = q_\alpha, \quad \alpha \in \{o, w\}, \tag{1}$$

where ϕ is the porosity, s_α is the saturation and q_α a source term for each phase α. The phase velocities $\mathbf{v}_\alpha$ are given by Darcy's law:

$$\mathbf{v}_\alpha = -\frac{k_{r\alpha}}{\mu_\alpha} \boldsymbol{K} \left(\nabla p_\alpha - \rho_\alpha g \nabla z\right), \quad \alpha \in \{o, w\},$$

where $\boldsymbol{K}$ is the absolute permeability, g is the gravity, z is height above a given datum and p_α, ρ_α, μ_α and $k_{r\alpha}$ are the phase pressures, densities, viscosities and relative permeabilities, respectively. In addition, we have the closing relation $s_w + s_o = 1$, and the capillary pressure $p_{\mathrm{cow}}(s_w) = p_o - p_w$. If we introduce the phase mobility $\lambda_\alpha = k_{r\alpha}/\mu_\alpha$, then

$$\mathbf{v}_o - \frac{\lambda_o}{\lambda_w} \mathbf{v}_w = -\boldsymbol{K} \lambda_o (\nabla p_{\mathrm{cow}} - \Delta\rho g \nabla z),$$

where $\Delta\rho = \rho_o - \rho_w$. Let $\mathbf{v} = \mathbf{v}_o + \mathbf{v}_w$ be the total Darcy velocity, and substitute $\mathbf{v}_o$ with $\mathbf{v} - \mathbf{v}_w$ in the above equation to obtain

$$\mathbf{v}_w = \frac{\lambda_w}{\lambda_w + \lambda_o} \mathbf{v} + \boldsymbol{K} \frac{\lambda_w \lambda_o}{\lambda_w + \lambda_o} (\nabla p_{\mathrm{cow}} - \Delta\rho g \nabla z).$$

This expression for $\mathbf{v}_w$ is then inserted into the water equation (1), where we now disregard sources and sinks. By observing that combining (1) and $s_w + s_o = 1$ yields $\nabla \cdot v = 0$, we obtain

$$-\phi \frac{\partial s_w}{\partial t} = \nabla f_w \cdot \mathbf{v} + \nabla \cdot \Big(\boldsymbol{K} \lambda_o f_w (\nabla p_{\mathrm{cow}} - \Delta\rho g \nabla z) \Big), \tag{2}$$

where $f_w = \lambda_w/(\lambda_w + \lambda_o)$. In the absence of gravity and capillary pressure, the fractional flow of water is equal to f_w. Equation (2) is a useful formulation for considering the influence of the different forces, as we discuss in the following.

3 Limiting Solutions

In this section, we will investigate the two limiting solutions of the simulation of the flooding of a reservoir, given by high flow rates and negligible flow rates.

3.1 High-Rate Limit

Whereas capillary and gravity forces are not affected by flow rate, the viscous forces increase with flow rate. This can be seen from (2), where the flow rate is only contained in the viscous term $\nabla f_w \cdot \mathbf{v}$. For high enough flow rates, the viscous term will dominate the capillary and gravity terms, such that $\nabla f_w \cdot \mathbf{v} \gg \nabla \cdot [\boldsymbol{K}\lambda_o f_w(\nabla p_{\text{cow}} - \Delta\rho g \nabla z)]$, and (2) can be reduced to the following form:

$$-\phi\frac{\partial s_w}{\partial t} = \nabla f_w \cdot \mathbf{v}. \tag{3}$$

As the fluids are assumed to be incompressible, flow rates $\mathbf{v}$ scale linearly with well rates q, which can be seen from (1). Therefore, simulations with different well rates yield the same flooding pattern. This only holds when we use (3) when scaled versus rate. To find this high-rate (viscous-dominated) limit solution, a simulation is run where the capillary pressure p_{cow} and density difference $\Delta\rho$ (and hence the influence of gravity) are both set to zero.

3.2 Low-Rate Limit

We now present a method for computing the production curves for a model, as function of injected water, in the limit of vanishing flow rates. This is a semi-analytical solution, giving us a fast and robust way of finding the low-rate results. This gives an alternative to running numerical simulations with very low velocities, which are often unstable and time-consuming.

With diminishing flow rates, we have $\nabla f_w \cdot \mathbf{v} \to 0$, and the capillary forces and gravity eventually become dominant. At steady state, when $\frac{\partial S_w}{\partial t} \to 0$, Eq. (2) is then reduced to

$$\nabla \cdot \Big[\boldsymbol{K}\lambda_o f_w(\nabla p_{\text{cow}} - \Delta\rho g \nabla z)\Big] = 0.$$

This equation is fulfilled if

$$\nabla p_{\text{cow}} = \Delta\rho g \nabla z. \tag{4}$$

Thus, with diminishing flow rates the capillary and gravity forces will be in equilibrium at all times. Note that this means equilibrium in all directions, in contrast to vertical equilibrium (Yortsos 1995).

To construct a semi-analytical solution for this limit, consider a discretized three-dimensional reservoir model with N grid cells. Let $\hat{p}_{\text{cow}}$ be the capillary pressure at some reference height $z = \hat{z}$, and for each grid cell $i \in [1, \ldots, N]$, let s_w^i be the water saturation, z^i the height of the cell centroid, ϕ^i its porosity and V^i its volume. Given an average saturation s_w^* for the whole domain, we can solve (4) discretely on the grid using the following equations

$$p_{\text{cow}}^i(s_w^i) = \hat{p}_{\text{cow}} - \Delta\rho g z^i, \quad i \in [1, \ldots, N], \qquad \frac{\sum_{i=1}^N s_w^i \phi^i V^i}{\sum_{i=1}^N \phi^i V^i} = s_w^*. \tag{5}$$

Solving (5) then yields a relationship between the average saturation s_w^* and the cell saturations s_w^i.

One could obtain a relationship between s_w^* and $\hat{p}_{\mathrm{cow}}$ by using the inverted capillary pressure curves to find average saturations s_w^* for different values of $\hat{p}_{\mathrm{cow}}$. However, in the algorithm we present below, s_w^* is the known value and $\hat{p}_{\mathrm{cow}}$ is unknown. If we use the method of inverting the capillary pressure curves, we would have to use interpolation to find the value of s_w^* we seek, leaving us without proper control of the error of $\hat{p}_{\mathrm{cow}}$ and s_w^i. Therefore, we instead write the $N + 1$ equations (5) on residual form as $F(x) = 0$, and then use Newton iterations $x^{n+1} = x^n - J^{-1}(x^n)F(x^n)$, where J is the Jacobian of F. The iterations are continue until the residual $F(x^n)$ is below a preset tolerance level. As these calculations are relatively fast to compute, we have chosen a very low tolerance of 10^{-10}.

For (5) to have a solution, the capillary pressure functions $p_{\mathrm{cow}}^i(s_w^i)$ must yield pressures in the required range. Typically, this can be obtained by using functions with asymptotes at the end points. The special case when only gravity forces are present needs to be handled separately. The oil–water contact will then be a sharp interface at some height, and this height is simply computed from the mean water saturation s_w^* and the pore volume, yielding the sought fluid distribution for each grid cell.

As we now are able compute the relationship between the average saturation and the saturation distribution in the domain at any given time, we are in turn able to calculate the total production as a function of the amount of injected fluids. Consider some three-dimensional model of the reservoir, with any number of injection and production wells. Let the total injection rate of water and oil be given as r_{inj}^w and r_{inj}^o, respectively. Oil injection is also included as a possibility because the domain we consider could be part of a larger field, and so injection of fluids may either be well injection, or flow across the boundaries of our domain from other regions of the field. However, in this paper we only consider water injection. Denote the total production of phase α by P_α and the total injection by I_α.

Given any valid initial average water saturation $s_{w,0}^*$ in the domain (e.g., given by the irreducible water saturation), we iterate forward in time to compute the production. At each iteration, the net change in the total water volume is the found by the difference between injected and produced volumes, and the resulting saturation distribution is assumed to fulfill (5). Due to incompressibility, the reservoir volume produced is matched by the injection volume. For each iteration k, the following steps are performed;

(i) Find the cell saturations $s_w^i = s_w^i(s_{w,k}^*)$ by solving (5).

(ii) Given the saturation distribution, calculate the relative phase flow m_α for the sinks by taking a well index weighted sum over all sink cells

$$m_\alpha = \frac{\sum_i \mathrm{WI}^i \lambda_\alpha^i}{\sum_i \mathrm{WI}^i}, \qquad \alpha \in \{o, w\}, \tag{6}$$

where WI^i is the well productivity index of cell i, and the sums go over all sink (production well) cells in the domain. We use the Peaceman expression for the well index (Peaceman 1983). For a regular grid where all cells have the same height and also the wellbore radius is equal for all production cells, (6) simplifies to $m_\alpha = \sum_i K^i \lambda_\alpha^i / \sum_i K^i$. Using these phase flow values, we can compute the fractional flow for the sinks as

$$f_{s,\alpha} = \frac{m_\alpha}{m_w + m_o}, \qquad \alpha \in \{o, w\}.$$

(iii) Compute the total injected fluid volume during the current iteration

$$\Delta V_k = \Delta V_{o,k} + \Delta V_{w,k} = r_{\mathrm{inj}}^o \Delta t_k + r_{\mathrm{inj}}^w \Delta t_k,$$

where $\Delta t_k = t_k - t_{k-1}$ is the time step from previous iteration (see comment on time below). Note that in the examples herein, we only consider water injection, so $\Delta V_{o,k} = 0$. With the total injected fluid volume found, the total produced amount of phase α during the current iteration is given by $f_{s,\alpha} \Delta V_k$.

(iv) Update the total production

$$P_{\alpha,k} = P_{\alpha,k-1} + f_{s,\alpha} \Delta V_k, \qquad \alpha \in \{o, w\},$$

and the total injection

$$I_{\alpha,k} = I_{\alpha,k-1} + \Delta V_{\alpha,k}, \qquad \alpha \in \{o, w\},$$

as well as the average saturation

$$s^*_{w,k+1} = s^*_{w,k} + \frac{\Delta V_{w,k} - f_{s,w} \Delta V_k}{\sum_i \phi^i V^i}.$$

Then continue to next iteration.

The resulting production curves P_w and P_o are independent of the magnitude of the total injection rate $r^w_{\text{inj}} + r^o_{\text{inj}}$ and the time steps Δt_k. However, the step sizes Δt_k must be chosen small enough to limit error in the production curve. We have set the value of this step size by reducing Δt_k until the solution does not change notably. This semi-analytical solution is quasi-static. As we are in the low-rate limit, the fluids are given infinite time to redistribute, but the simulation is still dynamic as the saturations move forward in time at each iteration. Thus, in this limit, the concept of time is not properly defined, and the time steps Δt_k do not correspond to a physical reservoir time. However, this method provides us with the production rates as a function of the injection rates and serves as the lower limit solution for rate dependent simulations.

The saturation distribution found at each iteration would equal the steady-state solutions for vanishing flow rates, if these solutions could be obtained. However, to find the steady-state solutions would be computationally demanding, and often not possible in practice. Using this low-rate solution, method is on the other hand simple and fast. The low-rate solution is applicable to general heterogeneous models, including three-dimensional grids. Note also that more complex wells than presented here could be implemented by e.g., incorporating hydrostatic pressure fall in the wells. We will use the high-rate and diminishing-rate solutions described above to investigate the rate-dependent balance of forces for several flooding processes.

4 Upscaling

The single- and two-phase methods we use for upscaling, which are presented below, including the viscous- and capillary-limit cases, are described in several papers, see e.g., Christie (2001), Dale et al. (1997), Ekrann and Aasen (2000) and Pickup et al. (2000). In the following, we will let superscript '$*$' denote an upscaled value (which may be a scalar or a tensor), such that e.g., $\boldsymbol{K}^*$ denotes the upscaled value of the permeability field $\boldsymbol{K}$. We present the upscaling methods by considering a general domain Ω of a fine grid that is to be upscaled to a single coarse grid block Ω^c.

4.1 Single-Phase Upscaling

For a single phase, Darcy's law $\mathbf{v} = -(\boldsymbol{K}/\mu)\nabla p$ and the continuity equation $\nabla \cdot \mathbf{v} = 0$ give, assuming the viscosity is constant, the Laplace equation

$$\nabla \cdot (\boldsymbol{K}\nabla p) = 0. \tag{7}$$

The solution of this equation depends on the choice of boundary conditions applied. Assume first that fixed (Dirichlet) boundary conditions are applied. For each direction $d \in \{x, y, z\}$, a pressure drop Δp is applied across the domain Ω, and the pressure equation (7) is solved to obtain the pressure p, and thereby also the flux field $\mathbf{v}_d$. Let $\bar{v}_d$ then be the average flux through any cross section perpendicular to the direction of the pressure drop. The upscaled permeability in direction d is then given by

$$\boldsymbol{K}^{*,d} = -\frac{L_d}{\Delta p}\bar{v}_d, \tag{8}$$

where L_d is a representative distance between the inflow and outflow boundaries. This upscaling is performed in turn for each direction, and the upscaled permeability becomes a diagonal tensor

$$\boldsymbol{K}^* = \mathrm{diag}(K^{*,x}, K^{*,y}, K^{*,z}).$$

Herein, we apply Dirichlet boundary conditions in the flow direction with no-flow boundary conditions elsewhere, and thus get upscaled diagonal permeability tensors. If periodic boundary conditions are chosen instead, the upscaled permeability becomes a full 3×3 tensor as cross-flow may be present (Durlofsky 1991).

4.2 Two-Phase Upscaling

It is well known that two-phase upscaling is rate dependent, with capillary forces dominating for small grid scales, and capillary and gravity forces dominating at low flow rates, while viscous forces dominate for large grid scales and at high rates (Ekrann and Aasen 2000). We consider upscaling in the rate limits, where the situation can be simplified, whereas upscaling at intermediate flow rates is not considered herein.

The first step of a steady-state two-phase upscaling is calculating the saturation distribution $\hat{s}_w$ at steady state. For the *capillary-limit* (or *capillary/gravity-limit*) upscaling method, this distribution is found by solving (5) for some given value of the average saturation s_w^*. Then, the phase permeabilities $\widetilde{\boldsymbol{K}}_\alpha = k_{r\alpha}(\hat{s}_w)\boldsymbol{K}$ are computed, and we apply single-phase upscaling as explained above to obtain upscaled (effective) phase permeabilities $\widetilde{\boldsymbol{K}}_\alpha^{*,d}$. The upscaled relative permeabilities are then computed as

$$k_{r\alpha}^{*,d}(s_w^*) = \frac{\widetilde{\boldsymbol{K}}_\alpha^{*,d}}{\boldsymbol{K}^{*,d}}. \tag{9}$$

The capillary pressure is also upscaled using the same saturation distribution $\hat{s}_w$. In the solution of (5), the capillary pressure is constant at each height of the domain, and a natural choice for the upscaled capillary pressure value is to select the capillary pressure at the coarse cell centroid height z_c. That is,

$$p_{\mathrm{cow}}^*(s_w^*) = \hat{p}_{\mathrm{cow}} - \Delta\rho g \left(z_c - \hat{z}\right),$$

where we recall that $\hat{p}_{\mathrm{cow}}$ is the capillary pressure at the reference height $\hat{z}$. Note that if we choose the characteristic height in (5) to be $\hat{z} = z_c$, then simply $p_{\mathrm{cow}}^*(s_w^*) = \hat{p}_{\mathrm{cow}}$. This process of upscaling relative permeability and capillary pressure is repeated for different values s_w^* to obtain full upscaled curves. The upscaling is also performed for each spacial dimension. Note that we normally refer to this method by the term *capillary-limit* upscaling, but the upscaling also accounts for gravity forces if they are present.

The *viscous-limit* upscaling method assumes that viscous forces dominate, and (3) applies. Assuming steady state, the time derivative of the saturation goes to zero and (3) further reduces to

$$\nabla f_w \cdot \mathbf{v} = 0. \tag{10}$$

Thus, the fractional flow is constant along streamlines, and the solution to (10) depends on the distribution of fractional flow over the inlet face of the coarse grid block. In particular, this means the solution is not unique. A common choice is to assume a constant fractional flow on the whole inlet boundary, resulting in constant fractional flow throughout the coarse grid block (Dale et al. 1997). With this assumption, the saturation distribution for each fractional flow value $\hat{f}_w$ is obtained by inverting the fractional flow function f_w, such that $\hat{s}_w = f_w^{-1}(\hat{f}_w)$. Similar to the diminishing-rate limit, once the saturation distribution is found, we apply single-phase upscaling for the phase permeabilities $\widetilde{\boldsymbol{K}}_\alpha = k_{r\alpha}(\hat{s}_w)\boldsymbol{K}$ to obtain upscaled (effective) phase permeabilities, and then, the upscaled relative permeabilities are computed from (9). This process is repeated for different fractional flow values $\hat{f}_w$ to obtain upscaled relative permeabilities for different values of the corresponding average saturation. We set the upscaled capillary pressure equal zero for the viscous-limit upscaling.

5 Simulation Examples

We will investigate how gravity, capillary pressure and viscous forces are present at different flow rates during a water flooding of a reservoir. In particular, we investigate at what rates each of these forces can be ignored, and thus find when the limiting solutions are valid. To this end, we consider different simplified examples of water flooding of an oil-filled reservoir. We first use a homogeneous 1D example to investigate the balance of capillary versus viscous forces in the direction of flow. Then, we extend the homogeneous model to 2D to investigate the balance of gravity versus viscous forces. Finally, to investigate the capillary (and gravity) redistribution of fluids both perpendicular and along the flow direction, we add heterogeneities by assigning different rock types to different layers.

The three forces considered will generally depend nonlinearly on each other and are thus not truly separable. However, to quantify at what flow rates, each force has significant impact on the solution, we simplify and consider the effects of the forces separately.

5.1 General Model Description

The example models considered in this section are all derived from the same base case that is of physical dimensions $2000 \times 5 \times 20$ m and has a grid size of $400 \times 1 \times 20$ cells. Sketches of two different variations are shown in Fig. 1. There are two rock types used, a higher permeable rock (type 1) with permeability $K_1 = 1000$ mD, and a lower permeable rock (type 2) with $K_2 = 10$ mD. The permeability within each rock type is homogeneous and isotropic, and the porosity is constantly equal $\phi = 0.25$ for the entire domain. Depending on the example, we use either equal mobilities and linear relative permeabilities,

$$\mu_o = 1.0\,\text{cP}, \quad \mu_w = 1.0\,\text{cP}, \quad k_{rw}(s_w) = \widetilde{s}_w, \quad k_{ro}(s_w) = 1 - \widetilde{s}_w. \tag{11}$$

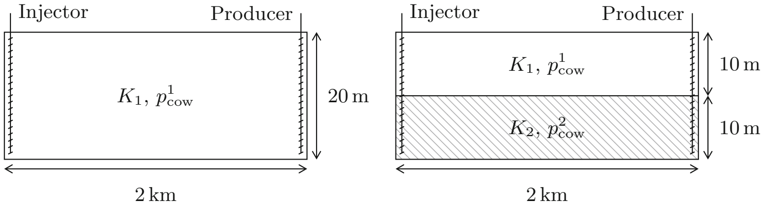

Fig. 1 Sketches of two of the models considered in the examples. *Left* Homogeneous model. *Right* Model with two horizontal layers

or different phase viscosities and quadratic relative permeability curves,

$$\mu_o = 1.5\,\mathrm{cP}, \quad \mu_w = 0.5\,\mathrm{cP}, \quad k_{rw}(s_w) = 0.5(\widetilde{s}_w)^2, \quad k_{ro}(s_w) = (1-\widetilde{s}_w)^2, \tag{12}$$

where $\widetilde{s}_w(s_w) = (s_w - s_{wir})/(1 - s_{wir} - s_{or})$. The same relative permeability functions apply to both rock types, the irreducible water saturation is $s_{wir} = 0.1$ and the residual oil saturation $s_{or} = 0.1$ and the initial water saturation is set equal the irreducible water saturation in the entire domain for all simulations. If nothing else is stated, then the densities are set to $\rho_o = 925\,\mathrm{kg/m^3}$ and $\rho_o = 1025\,\mathrm{kg/m^3}$. The capillary pressure curves are computed from a Leverett J-function, such that

$$p_{\mathrm{cow}}(s_w) = J(s_w)\gamma\cos\theta\sqrt{\phi/K}, \tag{13}$$

where $J(s_w)$ is the Leverett J-function, γ is the surface tension and θ is the contact angle between water and oil, ϕ is porosity and K is permeability. For the examples herein, we have chosen to use $\gamma = 0.022\,\mathrm{N/m}$ and $\theta = 45°$. The J-function we use is from tabulated data, and the resulting p_{cow} curve for rock type 1 ($\phi = 0.25$, $K = 1000\,\mathrm{mD}$) is shown in Fig. 4.

An injection well is included at the west end of the model, and a producer is included at the east end. For each model variation considered, simulations are performed for a series of different injection rates. Throughout each of these simulations, the wells are injecting and producing at a constant rate until 2 PV (pore volumes) of water have been injected.

5.2 Homogeneous 1D Example

We start by investigating the force balance in a 1D homogeneous horizontal case. Since all grid cells have the same height above datum, there will be no contribution of gravity. The only competing forces are then the viscous and capillary forces and (2) simplifies to

$$-\phi\frac{\partial S_w}{\partial t} = \nabla f_w \cdot \mathbf{v} + \nabla\cdot\left(\boldsymbol{K}\lambda_o f_w \nabla p_{\mathrm{cow}}\right). \tag{14}$$

Even though we discuss a 1D case in this section, we choose to keep equation 14 in general 3D form for better comparison with the other example cases.

The homogeneous 1D model has the same physical dimensions as the general model and consists only of rock type 1, such that the permeability is $K_1 = 1\,\mathrm{D}$ in the entire domain. In this example, the viscosities are unequal and the relative permeabilities are quadratic, as given by (12).

To investigate the balance of forces, we run simulations for a range of different injection rates. The flow rate through the domain is represented by the *interstitial (seepage) velocity* $u = v/\phi = Q/(A\phi)$, where Q is the injection rate and $v = Q/A$ is the corresponding Darcy velocity (specific discharge). Thus, the interstitial velocity gives flow in the units of length

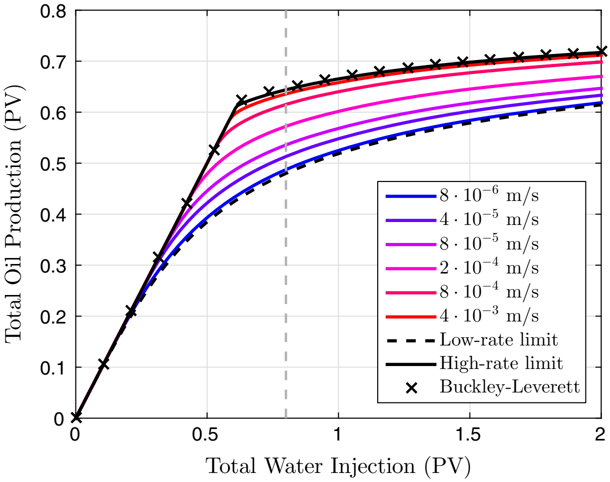

Fig. 2 Total oil production for the homogeneous 1D model of length 2000 m for different interstitial velocities

per time, and we use m/day. To maintain approximately the same numerical accuracy, the time steps are adjusted relative to the flow rate, such that the same number of time steps are used in all simulations.

Some of the resulting total oil production curves are plotted as a function of total injected water for different interstitial velocities in Fig. 2, where also the limiting solutions are shown. These limits are computed as described in Sect. 3. We observe that the rate-dependent solutions converge to the low-rate (capillary dominated) limit for small rates and to the high-rate (viscous-dominated) limit for large rates. The high-rate limit is similar to the Buckley–Leverett solution (Buckley and Leverett 1942), which is plotted as cross-marks in Fig. 2 for comparison.

To better visualize the transition of the solution between the low-rate and high-rate solution limits, and also to see at what rates the solution converges, another comparison of the simulations is shown in Fig. 3. Here, the total oil production is plotted as a function of the velocity at the point where 0.8 PV (pore volume) of water has been injected into the domain. In other words, Fig. 3 shows the intersection of the curves in Fig. 2 at the point indicated by the dotted vertical line. The results for two shorter models are also included in Fig. 3 to show how the results depend on the model length.

At low injection rates, the viscous term $\nabla f_w \cdot \mathbf{v}$ in (14) will go toward zero as $|\mathbf{v}| \to 0$. Then, the capillary forces are given enough time to redistribute the fluids throughout the domain, resulting in the capillary forces being in equilibrium. For the homogeneous model, this means that the saturation will be close to constant in space at each point in time. Considering Fig. 3, we see that the rate-dependent solutions converge toward the low-rate limit as the flow velocity decreases. However, for the 2000 m model, the velocity needs to be as low as 10^{-6} m/day for the rate-dependent solutions to converge to the calculated low-rate limit. Note that the velocities at which the rate-dependent solutions converge will depend on the absolute permeability of the system, as seen in "Capillary Number" section.

For high enough injection rates, on the other hand, the Darcy velocity $\mathbf{v}$ in equation (14) becomes so large that $\nabla f_w \cdot \mathbf{v} \gg \nabla \cdot (\boldsymbol{K}\lambda_o f_w \nabla p_{\mathrm{cow}})$, and the viscous forces dominate the

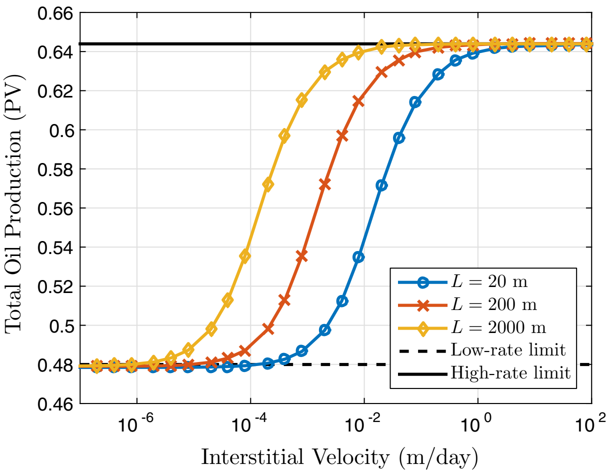

Fig. 3 Total oil production after 0.8 PV of water injection (at *vertical line* in Fig. 2) for homogeneous 1D model of different lengths

flow. We see in Fig. 3 that the rate-dependent solutions converge to the high-rate limiting case, and the transition going from the low-rate to the high-rate limit is relatively smooth.

The time needed for the capillary forces to redistribute the fluids is proportional to the length the fluids need to be transported. Thus, when the length of the model is reduced by one order of magnitude, e.g., from 2000 to 200 meters, the time needed to redistribute the fluids is reduced by one order of magnitude too. This is clearly seen in Fig. 3, where the solutions for three different model lengths are plotted. All three models have the same number of grid cells, and thus, the size of each cell changes with the model length.

A realistic interstitial velocity for water flooding of an oil reservoir is in the order of 1 m/day (Chen et al. 2001). In Fig. 3, we observe that all three model lengths are in the viscous-dominated regime for this velocity. However, by just considering the plot, it does seem like models shorter than 20 meters start to move away from the high-rate limit for an interstitial velocity of 1 m/day. If the same trend continues, we need models shorter than approximately 2 mm to be at the low-rate limit solution for realistic velocities. Note that this length is for an isolated domain, giving a maximum possible change of water saturation through the simulation. Also, note that this is not a length restriction for capillary-limit *upscaling*. As we will see in later examples, capillary-limit upscaling may be valid for flow rates larger than the low-rate limit solution.

This force balance depends on relative permeability, capillary pressure curves and the viscosity of the fluids. Still, for realistic flow parameters, viscosities and flow rates we cannot assume capillary equilibrium in the flow direction for typical reservoir models.

5.2.1 Capillary Number

It is common to use a capillary number to describe the ratio between capillary and viscous forces (Zhou et al. 1997); however, there exists several different such numbers (Lake 1989). The capillary number can be considered scale dependent as discussed in Odsæter et al. (2015), where the authors consider the capillary number in the context of steady-state upscaling.

Considering the terms in Eq. (14), we define a capillary number N_c as

$$N_c = \frac{\widetilde{f_w}\widetilde{v}}{\widetilde{K}\widetilde{\lambda_o}\widetilde{f_w}\widetilde{\nabla p_{\mathrm{cow}}}} = \frac{\widetilde{v}}{\widetilde{K}\widetilde{\lambda_o}\widetilde{\nabla p_{\mathrm{cow}}}}, \tag{15}$$

where the tilde indicates that the values are somehow representative for the particular case considered. For simplicity, we assume the relative permeability for oil is one, such that $\widetilde{\lambda_o} = 1/\mu_o$.

The characteristic number $\widetilde{\nabla p_{\mathrm{cow}}}$ for the capillary pressure change in the domain is constructed as follows. Given the capillary pressure function $p_{\mathrm{cow}}(s_w)$, divide its domain into N intervals of equal length, such that interval i is $[s_w^i, s_w^{i+1}]$, and thus, $s_w^1 = s_{wir}$ and $s_w^{N+1} = 1 - s_{or}$. On each interval, compute the the discrete slope of the function by

$$d^i = \frac{p_{\mathrm{cow}}(s_w^{i+1}) - p_{\mathrm{cow}}(s_w^i)}{s_w^{i+1} - s_w^i}, \qquad i = 1, \ldots, N.$$

Let M be the median of all the discrete slopes d^i, and let L be the length of the domain we consider. We then define

$$\widetilde{\nabla p_{\mathrm{cow}}} = \frac{\Delta p_{\mathrm{cow}}}{L} = \frac{(1 - s_{or} - s_{wir})|M|}{L}.$$

Note that we choose the median and not the mean, because we do not want extreme asymptotes at the ends to dominate.

For the 1D homogeneous example discussed just above, the constants appearing in N_c are given by $s_{wir} = 0.1$, $s_{or} = 0.1$, $\mu_o = 1.5\,\mathrm{cP}$, $\widetilde{K} = 1\,\mathrm{D}$, $M \approx -0.05\,\mathrm{bar}$ and the model length L varies. To illustrate how the number M relates to the capillary pressure, the line $p_c(s_w) = Ms_w + b$ is plotted on top of p_{cow} in Fig. 4, where b is chosen to minimize the distance from p_{cow}.

In Fig. 5, each of the three transition curves from Fig. 3 are plotted against the capillary number

$$N_c = \frac{\mu_o \widetilde{v} L}{\widetilde{K}(1 - s_{or} - s_{wir})|M|} \approx (4.40\,\mathrm{day/m^2}) v L,$$

where the velocity v is given in units of m/day (for direct comparison with Fig. 3), and the length L is given in meters. Note that the capillary number scales with the velocity. In addition, it will depend on the particular shape of the capillary pressure curves, and thus also the interfacial tension, which is kept constant in our examples.

We see that the capillary number $N_c = 1$ in the middle of the transition from low-rate to high-rate limit for each of the three model lengths. Also, we observe that the total oil production is independent of the model length when plotted against the capillary number. Thus, the capillary number N_c is reasonable for this example.

5.3 Homogeneous 2D Example

To consider gravitational forces, we now move to a two-dimensional model. Consider the base case of length 2000 m and height 20 m with 20 grid cells in the vertical direction. For simplicity, and to be able to study the effect of gravity, we ignore capillary forces. The competing forces are then the viscous and gravitational forces, and (2) simplifies to

$$-\phi \frac{\partial S_w}{\partial t} = \nabla f_w \cdot \mathbf{v} - \nabla \cdot (\boldsymbol{K}\lambda_o f_w \Delta\rho g \nabla z). \tag{16}$$

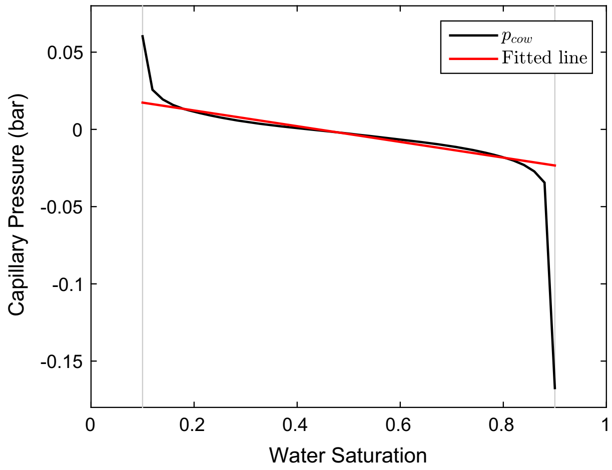

Fig. 4 Capillary pressure and the fitted line found from median slope fit

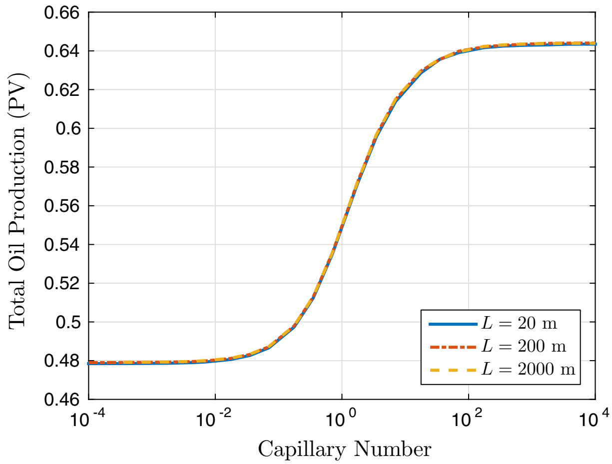

Fig. 5 Production from Fig. 3 plotted against the capillary number N_c

The simulations are once again run for a range of injection rates, and similar to the 1D case, we plot in Fig. 6 the total oil production after 0.8 PV of water has been injected. Three different values for the fluid density difference $\Delta\rho = \rho_w - \rho_o$, and both linear and quadratic relative permeability curves are considered. This gives six different cases, which are all plotted in Fig. 6. The low-rate and high-rate limit solutions in these plots are computed as described in Sect. 3.

We note that for the lowest injection rates, the simulations become numerically challenging because it is difficult for gravity alone to distribute the water in the horizontal direction. To be able to run these lowest rates, a small capillary pressure is added, which helps to distribute the water, but does not change the results notably.

Analogous to the balance between capillary and viscous forces in the previous example, the gravity will now be dominant for small enough injection rates, as can be seen from (16). At the low-rate limit, the saturations will be in vertical equilibrium. This gives a sharp oil–

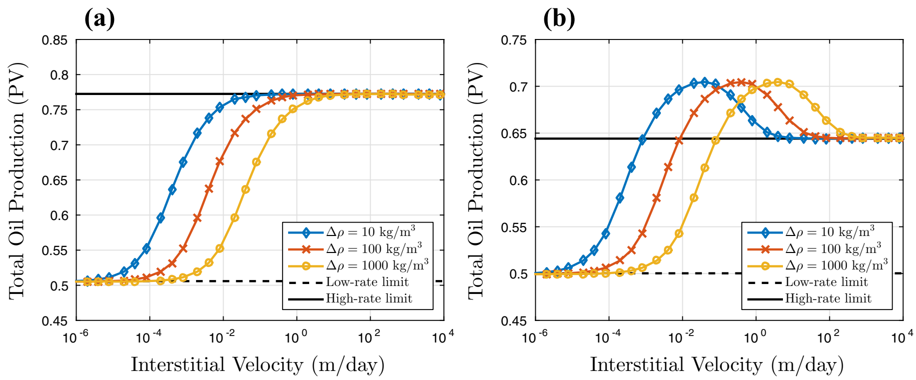

Fig. 6 Total oil production after injection of 0.8 PV of water for the homogeneous 2D model with gravity and without capillary pressure. Different fluid density differences $\Delta\rho = \rho_w - \rho_o$ are used. **a** Linear relative permeability, $\mu_o = \mu_w$. **b** Quadratic relative permeability, $\mu_o > \mu_w$

water contact at some height in the domain, with residual oil saturation below and irreducible water saturation above. This horizontal interface will gradually move upwards as the domain becomes water filled from the bottom up.

Considering simulations with increasing injection rates, starting from the low-rate limit, the viscous forces will become more dominant, and the flow gradually changes character to a piston-like flooding. This transition can be seen in both plots in Fig. 6, where the solutions move away from the low-rate solution limit and the total production increases. For rates above this transition, the water front in the case of linear relative permeability is a sharp vertical interface, such that almost all mobile oil has been produced at water breakthrough. We note that for linear relative permeabilities the high-rate limit converge to the the Buckley–Leverett solution. In the case of quadratic relative permeability, however, the highest production rates are not found at the high-rate limit solution. Instead, for simulations at the top of the transition curve, the water front is tilted, because gravity has time to segregate the fluids and create a gravity tongue as shown in Fig. 7a. Due to the fluid segregation, the saturation in the tongue is close to residual oil. When the velocity is increased further, gravity does not have time to separate the fluids, and the water front is perpendicular to the flow direction (Fig. 7b). As is well known from Buckley–Leverett solutions, significant amounts of oil is left behind the water front in this case due to the shape of the relative permeability curves, causing less oil to be produced. This reduction in total production for increased injection rates can be seen as the second transition from the top of the curve and down toward the high-rate limit as shown in Fig. 6b. In general, the shape of the relative permeability curves influence the transitions. As changes in wettability and pore structure alters the relative permeability, these properties will then affect the transition between low- and high-rate limits. Note again that the velocities where the transition converges to the limit solutions will depend on the absolute permeability of the system (see section in "Gravity Number").

For water and oil, a typical density difference $\Delta\rho = \rho_w - \rho_o$ can be approximately 150 kg/m^3. For a realistic interstitial velocity of 1 m/day, we see in Fig. 6 that we are at the high-rate limit solution in the case of linear relative permeability curves, but not for quadratic curves. If the trend of the density difference continues similarly, we need almost equal fluid densities to be at the high-rate limit at realistic flow rates with quadratic curves. Thus, in this example we cannot ignore the effect of gravity, and it seems like neither of the limit solutions are valid assumptions.

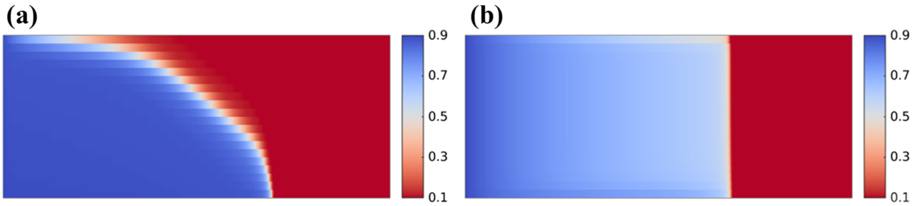

Fig. 7 Water saturation after injection of 0.4 PV of water for the homogeneous 2D model with gravity and without capillary pressure, using quadratic relative permeability, $\mu_o > \mu_w$, and $\Delta\rho = 10\,\text{kg/m}^3$ for two different velocities. **a** Interstitial velocity 0.04 m/day, at the top of the transition curve in Fig. 6b. **b** Interstitial velocity 8 m/day, to the right of the transition, at the high-rate limit in Fig. 6b

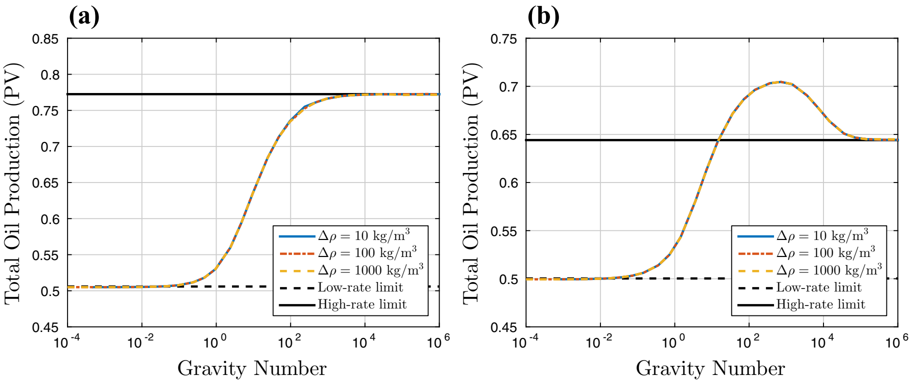

Fig. 8 Same results as in Fig. 6, now plotted against the gravity number N_g as given by equation (17). **a** Linear relative permeability, $\mu_o = \mu_w$. **b** Quadratic relative permeability, $\mu_o > \mu_w$

5.3.1 Gravity Number

In a similar fashion as a capillary number was defined in the previous section, we now define a gravity number. Considering the terms in equation (16), we define a gravity number N_g as

$$N_g = \frac{\widetilde{f_w}\widetilde{v}}{\widetilde{K}\widetilde{\lambda_o}\widetilde{f_w}\Delta\rho g\widetilde{\nabla z}} = \frac{\widetilde{v}}{\widetilde{K}\widetilde{\lambda_o}\Delta\rho g\widetilde{\nabla z}}, \tag{17}$$

where, as before, the tilde indicates representative values.

For the homogeneous 2D model considered above, the parameters appearing in the gravity number N_g are given by $\widetilde{K} = 1000\,\text{mD}$, $\widetilde{\lambda_o} = 1/\mu_o$, $g = 9.8\,\text{m}/s^2$, and $\widetilde{\nabla z} = 1/100$ is chosen as the model height divided by the model length. In Fig. 8, the six curves in Fig. 6 are plotted versus the gravity number N_g. We observe that the curves almost fall on top of each other and that the gravity number $N_g = 1$ is inside the transition from gravity dominated to viscous dominated. Thus, the gravity number N_g as defined by (17) is reasonable for these examples.

5.3.2 Homogeneous Model with Gravity and Capillary Forces

To observe how capillary pressure affects the results, we now add capillary forces into the system. The capillary pressure is scaled with the density difference $\Delta\rho$ to obtain equal relative difference between capillary and gravity forces. If we let $\hat{p}_{cow}$ be the capillary pressure

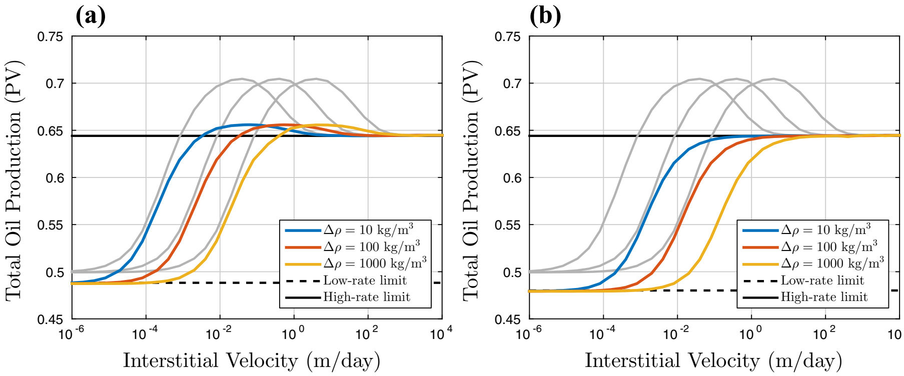

Fig. 9 Total oil production after injection of 0.8 PV of water for the homogeneous 2D model with gravity and capillary pressure p_{cow} as given in each caption, where the function $\hat{p}_{\mathrm{cow}}$ is computed from (13). The *curves* without any capillary pressure from Fig. 6b are shown in *gray* for comparison. **a** $p_{\mathrm{cow}} = \hat{p}_{\mathrm{cow}}|\Delta\rho|/10$. **b** $p_{\mathrm{cow}} = \hat{p}_{\mathrm{cow}}|\Delta\rho|$

function as defined by (13), then the capillary pressure is set to $p_{\mathrm{cow}} = \hat{p}_{\mathrm{cow}}|\Delta\rho|/10$ in Fig. 9a, and to $p_{\mathrm{cow}} = \hat{p}_{\mathrm{cow}}|\Delta\rho|$ in Fig. 9b (the limit solutions in these figures are computed as described in Sect. 3). Thus, for all the cases except $\Delta\rho = 10\,\mathrm{kg/m^3}$ in Fig. 9b, the capillary pressures are larger than the default values. In Fig. 9b, the capillary forces are ten times larger relative to gravity than in Fig. 9a. As the capillary forces increase relative to gravity, the diffusion increases both normal to and along the flow direction. In the vertical direction, the capillary forces will counteract gravitational segregation. In Fig. 9b, the capillary forces become so large that capillary diffusion dominate gravity, and the flow becomes essentially one dimensional. This can also be seen as the shape of the curves in Fig. 9b are similar to the one-dimensional results in Fig. 3.

5.4 Layered 2D Example

To investigate the balance between capillary and viscous forces perpendicular to the flow direction, we consider a 2D model consisting of horizontal layers of two different rock types. To isolate the forces arising from capillary pressure, we let the oil density be equal to the water density to remove gravity effects. We use equal viscosities and linear relative permeabilities as given by (11), causing equal total mobility in the two rock types. There is then no viscous cross-flow between the layers arising from total mobility contrast. The capillary pressure curves for the two rock types are computed from (13).

We consider three different models, where the physical size in all cases is $2000 \times 5 \times 20$ m, while the number of rock layers changes. Thus, the thickness of each layer is the height of the model divided by the number of layers. Alternate layers were of rock type 1 and 2, starting from the top with the high-permeable rock type 1. A sketch of the model with two layers is shown in Fig. 1. The total number of grid cells in the vertical direction is chosen as 20 for the models with 2 and 20 rock layers, and 200 cells are used for for the model with 200 rock layers. Different resolutions have been tested, and though a higher grid resolution will slightly alter the results, the changes are small enough to not be of importance for this paper.

As in previous examples, simulations are carried out for a range of injection rates. The resulting total oil production after injection of 0.8 PV of water for the different layered models is plotted in Fig. 10, where also the capillary number N_c as defined by (15) is shown. This

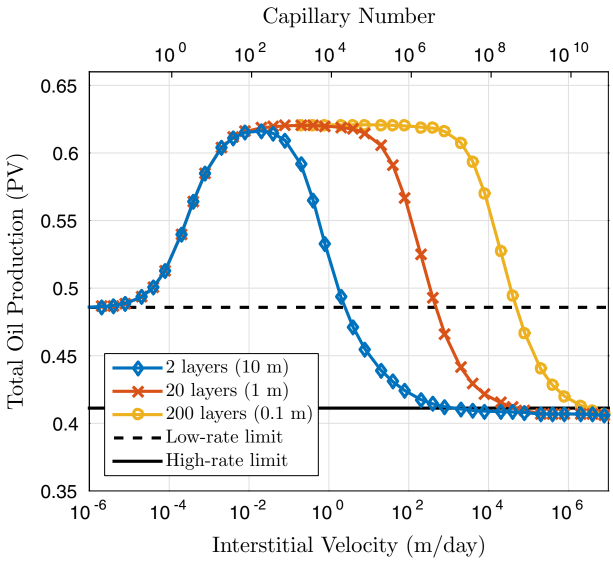

Fig. 10 Total oil production after injection of 0.8 PV of water for the horizontally layered models without gravity. The height of a single layer is written in parenthesis. The capillary number N_c as defined by (15) is given as a second x-axis on the *top*. Note that the velocities at which the rate-dependent solutions converge to the limit solutions depend on the effective (upscaled) absolute permeability of the model

plot reveals two distinct transitions. At interstitial velocities below 10^{-5} m/day, the capillary forces dominate the distribution of the fluids, and the solutions are seen to converge to the low-rate limit. That is, the capillary forces are both in vertical and horizontal equilibrium. When increasing the flow rate up toward 10^{-2} m/day, the viscous forces become dominant in the distribution of fluids in the direction of flow. However, the distribution of fluids perpendicular to the flow direction is still dominated by capillary forces, and we thus still have a vertical equilibrium. That there are different forces dominating along and perpendicular to the flow direction is mainly due to differences in lengths; the model length horizontally is much larger than the lengths between the layers in the vertical direction. Thus, the capillary pressure uses less time to redistribute the fluids vertically between the layers than horizontally along the layers. For velocities around 10^{-2} m/day, this results in a piston-like flooding scenario where capillary forces are in equilibrium normal to the flow direction. In Fig. 10, we observe that the transition from capillary equilibrium in both directions to a plateau where we only have equilibrium normal to the flow direction is similar for different number of layers. This is in accordance with the capillary number also included in Fig. 10, as this dimensionless number describes the balance of viscous to capillary forces in direction of flow. This transition is similar to what was observed in the 1D homogeneous case plotted in Fig. 3; thus, the force balance in the direction of flow appears similar to the 1D homogeneous case.

The three models considered here all have equal volume of each of the two rock types, which causes the transition from capillary equilibrium to vertical equilibrium to be equal, and all three models end at the same plateau at 10^{-2} m/day. With even higher rates, the viscous forces become so large that capillary forces no longer have time to redistribute the fluids perpendicular to the flow direction. This is seen as the second transitions in Fig. 10, where the solutions go from vertical equilibrium at the plateau and down toward the high-rate limit. In this transition, the solutions move from a piston-like flooding with vertical equilibrium (perpendicular to the flow), to a scenario where the high-permeable layers are flooded before the low-permeable layers. This causes negligible production of oil from the low-permeable layers after injection of 0.8 PV of water, and therefore, the production at 0.8 PV seen in Fig. 10 drops from vertical equilibrium to the high-rate limit. As the constant total mobility ensures no viscous cross-flow between the layers at higher rates, all models have the same high-rate limit solution.

Observe that the transition from the plateau to the high-rate limit is different for the different layered models. When increasing the number of layers, the vertical distance between grid cells of different rock type is reduced. Increasing the number of layers thus increases the gradient of the capillary pressure $\nabla p_{\text{cow}} = \Delta p_{\text{cow}}/l$ by reducing the distance l between grid cells of different rock types. At the same time, we also reduce the distance the fluids need to be transported between the layers. Decreasing the distance l by an order of magnitude will then increase the capillary pressure gradient by an order of magnitude and at the same time reduce the transport distance by an order of magnitude. Consequently, increasing the number of layers by *one* order of magnitude will shift the transition from the plateau to the high-rate limit by *two* orders of magnitude. This is shown in Fig. 10.

We also see in Fig. 10 that with a layer thickness of approximately 1 m (model of 20 layers), the transition from the plateau to the high-rate limit starts at an interstitial velocity of just above 10 m/day. Thus, for a model with layers thinner than approximately 1 m, a typical reservoir flow rate is at the plateau where viscous forces dominate in direction of the flow, while capillary forces dominate perpendicular to the flow.

6 Upscaling Examples

In this section, we investigate the validity of steady-state upscaling methods. The models are upscaled from a fine grid to a coarse grid, and then, these upscaled parameters are used in simulations to observe how well they are able to reproduce the fine-scale flow and how large errors the upscaling introduces.

6.1 Upscaling the Horizontally Layered Models Without Gravity

Consider the layered models introduced above with 2, 20 and 200 horizontal layers. We upscale these models to a coarse grid of size $40 \times 1 \times 1$. In all three models, half the domain of each coarse grid block is filled by rock type 1 and the other half by rock type 2; therefore, the upscaled flow parameters will be identical.

As the layers are parallel to the flow direction, the upscaled absolute permeability is simply the arithmetic mean, such that $K^* = (1000\,\text{mD} + 10\,\text{mD})/2 = 505\,\text{mD}$. The relative permeabilities are upscaled using both the viscous- and capillary-limit methods and are shown in Fig. 11a together with the original input curves. Note that the viscous-limit upscaling reproduces the input curves, in contrast to the capillary-limit upscaling. The upscaled capillary pressure is shown in red in Fig. 11b.

As before, simulations are run using a range of injection rates to observe how well the upscaled curves reproduce the fine-scale results. The total oil production resulting from simulations with lower velocities using capillary-limit upscaled data is shown in Fig. 12a. The fine-scale solutions in the low- and high-rate limits (computed as described in Sect. 3) are shown for comparison, and we observe how the coarse simulations converge to the low-rate limit. In the high-rate limit solution, almost all flow happens in the high-permeable

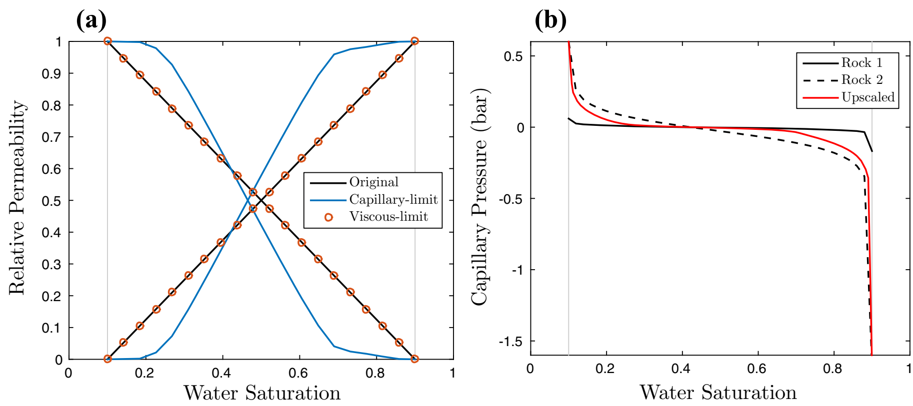

Fig. 11 Upscaled fluid properties for the horizontally layered models. **a** Relative permeability. **b** Capillary pressure

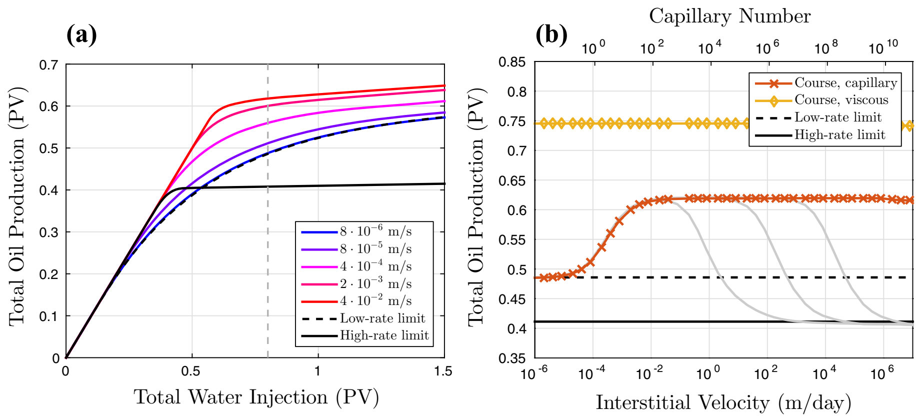

Fig. 12 Total oil production for the layered models without gravity. **a** Coarse-scale capillary-limit results. **b** Coarse-scale results after injection of 0.8 PV of water. Fine-scale results from Fig. 10 are shown in *gray*, and the capillary number N_c as defined by (15) is given as a second x-axis on the *top*

layers before water breakthrough. After the breakthrough, the remaining oil resides in the low-permeable layers only, which will take a very long time to produce.

To better visualize how the solutions depend on velocity, the total oil production for all solutions is plotted after injection of 0.8 PV of water in Fig. 12b. The capillary number N_c as defined by (15) is also shown. Again, the limit solutions in this plot are computed as described in Sect. 3. As there is no capillary pressure in the viscous coarse model, these results are rate independent when plotted against total injection. We also observe that the viscous-limit upscaling do *not* reproduce the fine-scale solution at the high-rate limit. The coarse results give approximately two times the total production compared to the fine scale. The reason for this mismatch becomes evident when considering the fractional flow during the flooding. For the fine-scale models, once the water saturation front has passed through in the high-permeable layers, the water fractional flow will be close to one in these layers and still close to zero in the low-permeable layers. The steady-state viscous-limit upscaling procedure assumes constant fractional flow inside each coarse grid block, and this assumption is clearly violated in this case. We therefore cannot expect the viscous-limit upscaling to capture the characteristics of the flow. However, if the coarse grid resolved the layered structure, i.e., if each coarse block only contained a single rock type, then the fractional flow would be close to constant within each block, away from the water front. In this case, the viscous-limit upscaling could be applied and would match the high-rate limit solution.

Another point about the high-rate limit is worth noting. In the high-rate limit, close to all flow in the fine-scale solution happens in the high-permeable layers, which adds up to only half the flow-area. For the coarse models, on the other hand, the flow is equal for the full area of the model. This causes the water front in the coarse model to move slower than in the fine-scale model, and water breakthrough happens at a later point in time. Thus, for this choice of coarse grid, both upscaling methods are incorrect for the high-rate limit, even before the water breakthrough.

Considering the results using capillary-limit upscaling in Fig. 12b, we see the coarse capillary simulations not only converge to the fine-scale low-rate limit, but also have the same transition from the low-rate limit and up to the plateau where the capillary forces are in equilibrium in the direction perpendicular to flow. At this plateau and for lower rates, the vertical fluid distribution is captured by the capillary-limit upscaling procedure. For higher flow rates, the viscous forces begin to influence the vertical fluid distribution, and this distribution is not captured by the upscaled model, as shown in Fig. 12b, where the upscaled results are unchanged when increasing the flow rates after reaching the plateau.

6.2 Upscaling Horizontally Layered Models with Gravity

In this subsection, we combine capillary and gravity forces and study the horizontally layered model with 20 layers. Three different density differences $\Delta\rho = \rho_w - \rho_o$ are used. The upscaled relative permeability and capillary pressure curves are shown in Fig. 13. When upscaling a gravity case, we observe how the gravity effect is included into both the upscaled relative permeability and capillary pressure curves. For the largest density contrast, the resulting capillary curve is dominated by the effect of gravity. This largest density difference can, however, not be considered realistic for petroleum reservoirs. Note that the horizontally layered model has alternate layers, starting with the high-permeable rock type at the top. The results in this section would be slightly different if the layer ordering was switched, but for as many as 20 layers, this difference is minimal.

The model is upscaled to a 1D grid of size $40 \times 1 \times 1$, and then simulations are run on the coarse scale. The total oil production after 0.8 PV water injected versus interstitial velocity is shown in Fig. 14a. As expected, the solution for the relatively low density difference of $10\,\mathrm{kg/m^3}$ in Fig. 14a is similar to the solution without gravity in Fig. 12b. As the gravity forces are increased, the shape of the transition changes.

To make Fig. 14a more readable, we do not include the viscous-limit coarse-scale results, but as for the results without gravity, the viscous-limit upscaling do not reproduce the fine-scale high-rate limit solution here either. The capillary-limit upscaling does, however, have a good match with the fine-scale results from the low-rate limit and up the point where viscous forces become dominant in the coarse simulations. Note that the low-rate limit is slightly different depending on the density difference, which reflects the change in the balance between gravity and capillary forces at this limit. At high rates, the coarse simulation reproduces vertical equilibrium, which seems to correspond to the top of the fine-scale simulation curves. Viscous influence on fluid distribution normal to the flow direction is not captured by the upscaled models; thus, the transition from vertical equilibrium to the high-rate limit solution

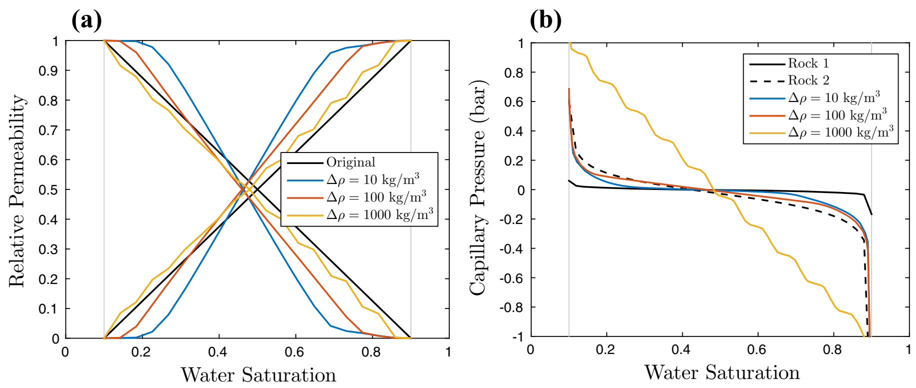

Fig. 13 Upscaled fluid properties for the horizontally layered model with 20 layers, including gravity and capillary pressure forces for different fluid density differences $\Delta\rho = \rho_w - \rho_o$. **a** Relative permeability. **b** Capillary pressure

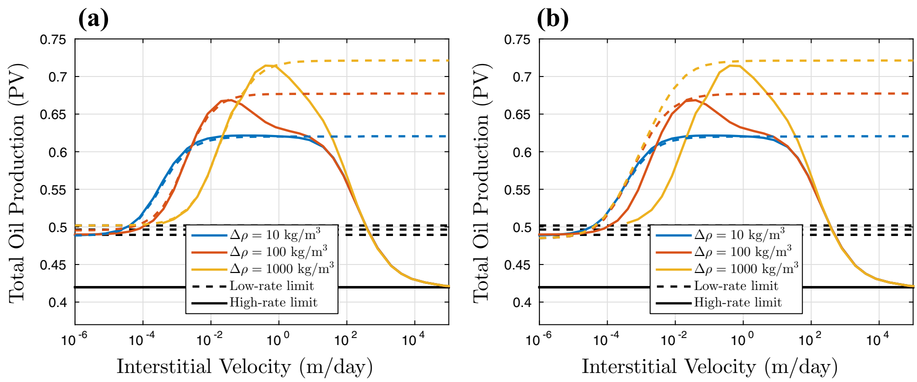

Fig. 14 Total oil production after injection of 0.8 PV of water injection for the model with 20 horizontal layers with capillary pressure and gravity for different fluid density differences $\Delta\rho = \rho_w - \rho_o$. Fine-scale results are shown in *solid lines*, and capillary-limit upscaling results are shown in *dashed lines*. Note that the fine-scale solutions are the same in both figures, but the coarse-scale results are different, **a** Default upscaling, **b** Disregarding gravity in p_{cow}-upscaling

is not captured by the upscaled models. Depending on the size of the density difference $\Delta\rho$, the coarse results match the fine-scale results up to around $0.01-1$ m/day.

To illustrate the effect of including the effect of gravity in the capillary pressure upscaling, the coarse results are shown in Fig. 14b where gravity has been disregarded when upscaling p_{cow}, but still included when upscaling relative permeability. We observe how the coarse models do not match the low-rate limit as the density difference increases, and the transitions toward higher flow rates are not matching the fine-scale simulations. This shows the importance of including gravity also in the capillary pressure upscaling.

7 A More Complex 2D Example

As the homogeneous and layered models are highly simplified, we would also like to consider a more complex model and see if we can generalize our conclusions. To this end, we consider

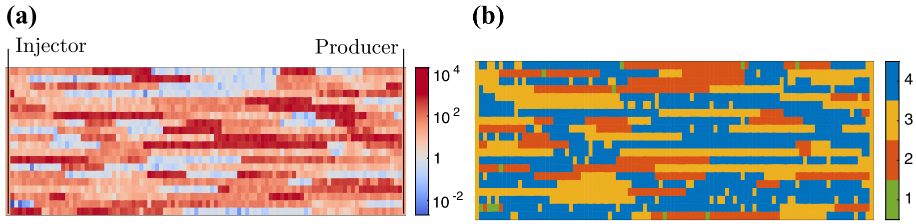

Fig. 15 SPE10 model 1. **a** Permeability field. **b** Rock types with $R = 4$ different types

model 1 of the 10th SPE Comparative Solution Project (Christie and Blunt 2001). The model has $100 \times 1 \times 20$ cells and physical dimensions $762 \times 7.62 \times 15.24$ m. To avoid any upscaling effects of the wells, extra cells with homogeneous porosity and permeability are added to both sides of the domain and the wells are then placed in these padding cells. The wells are shown together with the permeability field in Fig. 15. The porosity is $\phi = 0.2$ everywhere. The fluids are incompressible, with densities $\rho_o = 700\,\text{kg/m}^3$ and $\rho_w = 1025\,\text{kg/m}^3$, and viscosities $\mu_o = 1$ cP and $\mu_w = 0.5$ cP.

The original SPE10 model does not contain any capillary pressure data. As we want consider the balance between capillary, viscous and gravitational forces, capillary pressure curves are added into the model. We will compute the capillary pressure from the same Leverett J-function as before. This J-function is given as tabulated data, and the resulting p_{cow} curve for a rock type with $\phi = 0.25$ and $K = 1000$ mD is shown in Fig. 4. Now, to obtain different curves, the domain is divided into R rock types based on the value of $\sqrt{K/\phi}$, which is a factor in the capillary pressure function (13). For each cell i, we first define the number $q_i = \log_{10}(\sqrt{K_i/\phi_i})$, then let $\Delta q = (\max(q_i) - \min(q_i))/R$, and finally define the bins

$$Q_r = \left[\min(q_i) + (r-1)\Delta q, \min(q_i) + r\Delta q\right],$$

for $r = 1, \ldots, R$. Then, we let cell i be of rock type r if $q_i \in Q_r$. The capillary pressure of each rock type is computed from (13) with permeability taken as the log average and porosity as the average of all cells which is part of that rock type. We consider both the case of a single rock type ($R = 1$) and four different types ($R = 4$). The relative permeability is the same in the whole model and are quadratic Corey-type curves with end points $k_{ro}(0) = 1$ and $k_{rw}(1) = 0.5$.

Similar to what was done for the simpler models, we run the SPE10 model on the fine scale for a range of injection rates. Then, the model is upscaled both to a coarse grid with $25 \times 1 \times 1$ cells and one with $25 \times 1 \times 5$ cells, and the coarse models are then run for the same range of injection rates as the fine-scale model. Plots of the total oil production after 0.8 PV of water has been injected is shown in Fig. 16, both with a single capillary pressure curve ($R = 1$) and with four different curves ($R = 4$).

The first observation we make is that for both models, the fine-scale simulations and the upscaled capillary-limit simulations converge to the low-rate limits, as anticipated. The fine-scale solution converges to the low-rate limit for a velocity about 10^{-5} m/day and to the high-rate limit just below 10^2 m/day. We note that both these convergence rates and also the shape of the curves are quite similar to the homogeneous 2D case with quadratic relative permeability and $\Delta\rho = 100\,\text{kg/m}^3$, as shown in Fig. 6b, though the gravitational forces are now larger as $\Delta\rho = 325\,\text{kg/m}^3$.

The difference between a 1D coarse model and a coarse model with five cells in the vertical direction is clearly shown in Fig. 16. The 1D model does not include gravity in the coarse

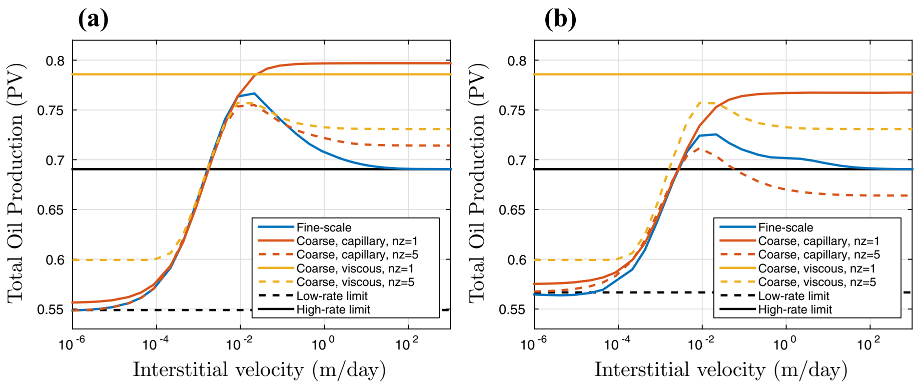

Fig. 16 Total oil production after injection of 0.8 PV of water for the SPE10 model 1, both upscaled to coarse grid with nz $= 1$ cell in vertical direction and nz $= 5$ cells. **a** A single p_{cow} curve ($R = 1$). **b** Four different p_{cow} curves ($R = 4$)

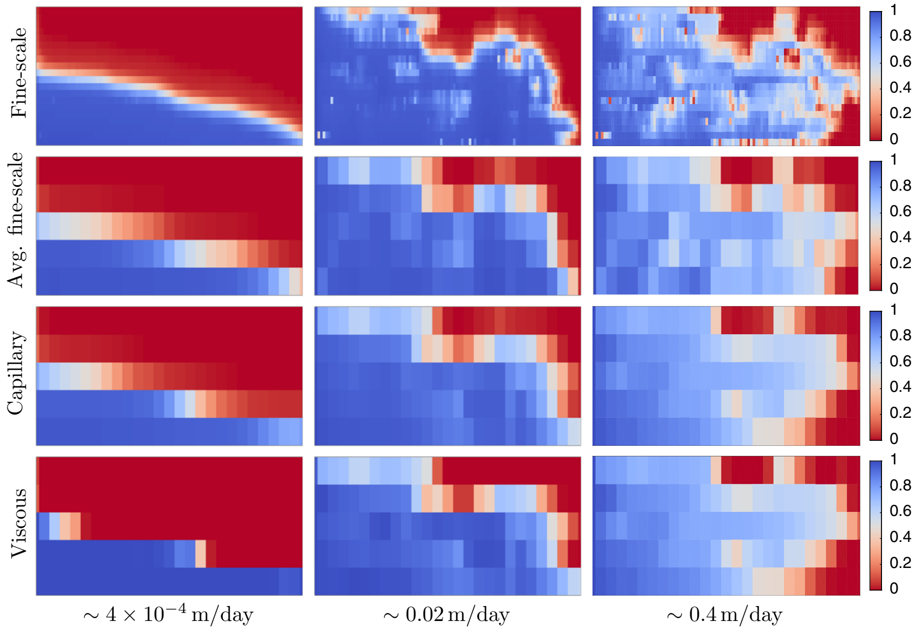

Fig. 17 Water saturation for SPE10 at the point of water breakthrough for different interstitial velocities and different models. The *second row* is the fine-scale results, averaged in each coarse block

simulation. In particular, this causes the viscous-limit upscaled model to be independent of rate when plotted versus injected volume, as seen before. The 1D capillary-limit coarse model behaves similar as for the upscaled horizontally layered model in Fig. 14a, following the fine-scale simulation from the low-rate limit and up to a point, before flattening out to a constant for higher velocities. Increasing the vertical coarse resolution to five cells, the match improves for both viscous- and capillary-limit coarse models. The saturation at water breakthrough is compared for these models in Fig. 17, where we observe that the gravity tongue now is reproduced in the coarse models. Here, we also see how the coarse capillary-limit results match the fine-scale better than the viscous-limit coarse results for the lower flow rate, while they are more similar for the higher flow rates.

8 Conclusion

In this article, we have introduced a semi-analytical solution for low-rate (capillary and gravity dominated) flooding of a reservoir. Together with the high-rate (viscous-dominated) limit, they give the solutions for the rate-dependent flooding process in the limit of vanishing or very large flow rates. For all models considered in this article, the fine-scale rate-dependent simulations converge to both the low-rate limit and the high-rate limit solutions, which indicates correctness of our semi-analytical low-rate solution. The rate-dependent simulations also show smooth transitions between these limits, though the transitions in general are neither trivial nor monotonic. Also, in all cases we have considered, either the low-rate or the high-rate limit provides a lower bound for the solution. However, the limits do not in general provide an upper bound. It is seen in Virnovsky et al. (2004) that there is a non-monotonous transition between the upscaled relative permeability curves in the capillary limit and viscous limit. In this paper, we observe that the fine-scale simulation results have a similar non-monotonicity.

The limit solutions allow us to understand when the rate-dependent simulations become close to the point where some forces are negligible and are in this way a useful tool in the discussion of force balance. Others have used dimensionless numbers to quantify when simulation results are close to the force balance limits and when simplified equations could be used, e.g., in Coats et al. (1967, 1971). Further work can be envisioned where the full transition from low-rate to high-rate limit solutions is used to validate dimensionless numbers, e.g., where such numbers are situated in the transition, and if they can be related to the length of the transition.

When considering a homogeneous 1D model, we only have driving forces in the flow direction. Our 1D model was clearly viscous dominated for realistic reservoir flow rates for model lengths down to 20 m. The cases considered indicate that for realistic flow parameters, viscosities, and flow rates, we cannot assume capillary equilibrium in the flow direction. We also suggested a dimensionless capillary number to describe the ratio of viscous to capillary forces in the flow direction, which also accounts for the model length. The capillary number was seen to be reasonable for the considered homogeneous 1D model.

To include the effect of gravity, we used homogeneous 2D models. It was seen that gravity forces were important at realistic reservoir rates, but they were not dominant. For quadratic relative permeabilities, we observed a non-trivial transition from gravity-dominated to viscous-dominated flow. This was explained by gravity having a positive impact on the production by reducing the oil saturation behind the water front. When capillary forces were included, the positive impact of the gravity was reduced as capillary forces were increased. Capillary forces counteract gravity segregation, so for large capillary forces relative to gravity, the displacement front becomes piston-like. This gives a transition which resembles the 1D model case.

The effect of capillary versus viscous forces for redistribution normal to the flow direction was investigated in horizontally layered models, where we disregarded gravity and used linear relative permeability curves to remove viscous cross-flow. The force balance in the direction of flow was similar to the 1D homogeneous case; thus, for realistic rates it was viscous dominated. Also, the force balance in the flow direction was not affected by the size of the layering, which is in contrast to the force balance normal to the flow direction. As lengths in the direction normal to flow commonly are several orders of magnitude smaller than lengths in the direction of flow, the force balance normal to the flow direction is typically close to capillary equilibrium, while viscous forces dominate the force balance along the direction of flow. At which thickness viscous forces start to influence the force balance normal to the flow will depend on different parameters, such as fluid properties and flow parameters.

When upscaling the horizontally layered models using capillary-limit upscaling, the coarse results reproduce the transition from the low-rate limit to vertical equilibrium. Thus, capillary-limit upscaling has validity outside the low-rate limit solution. For higher flow rates, the solution equals the vertical equilibrium solution. It was observed that for thin layers the capillary upscaling works well up to realistic flow rates, as the fine-scale solutions then are close to vertical equilibrium. Capillary-limit upscaling procedure thus seems fair for most situations when going from a lamina scale to a bed scale.

In the horizontally layered case, viscous-limit upscaling failed to capture the flow dynamics because the assumption of constant fractional flow was not valid. Though not included in this paper, we have investigated the upscaling of a vertically layered model. In this case, the fractional flow is constant in the direction normal to the flow, and we have seen that the viscous-limit upscaling reproduced the high-rate limit for such a model.

In general, the viscous-limit upscaling can be applied in cases where the fractional flow is relatively constant within each coarse grid block, away from the water front. When this assumption of constant fractional flow holds is highly case dependent, and is difficult to predict a priori for general models. For a horizontally layered model, the viscous-limit upscaling would be accurate if all the layers are resolved by the coarse grid resolution. In the case where layered heterogeneities are not resolved, the viscous-limit upscaling could still be applicable if the permeability contrast is small enough.

We also considered a horizontally layered model where gravity was included in addition to capillary forces. Depending on the fluid density difference, the capillary-limit upscaling was able to reproduce the transition from the low-rate limit and up close to realistic flow rates. The capillary-limit upscaling is applicable for highest flow rates when the gravitational forces are insignificant, e.g., upscaling to coarse blocks with limited vertical length.

Finally, we investigated the more complex SPE10, model 1, where we considered upscaling both to a one-dimensional coarse model and to a coarse model with five cells in vertical direction. Even with the heterogeneities of the model, similar results were seen as for the simpler models. The capillary-limit upscaling is able to reproduce the low-rate limit, as well as the transition up to flow rates where capillary and gravity forces no longer dominate the distribution of fluids normal to the flow direction. It was also observed that we can improve the coarse models by increasing the vertical grid resolution, as the coarse model is then able to capture more of the gravity effects.

Acknowledgments The research is funded by VISTA, which is a basic research program funded by Statoil and conducted in close collaboration with The Norwegian Academy of Science and Letters. The authors thank Knut-Andreas Lie and Vegard Kippe for helpful discussions.

References

Aarnes, J.E., Kippe, V., Lie, K.A., Rustad, A.B.: Modelling of multiscale structures in flow simulations for petroleum reservoirs. In: Geometric Modelling, Numerical Simulation, and Optimization, pp. 307–360. Springer, Berlin (2007)

Barker, J.W., Thibeau, S.: A critical review of the use of pseudorelative permeabilities for upscaling. SPE Reserv. Eng. **12**(2), 138–143 (1997)

Bear, J.: Dynamics of Fluids in Porous Media. Dover Publications, Mineola (1988)
Buckley, S., Leverett, M.: Mechanism of fluid displacement in sands. Trans. AIME **146**(1), 107–116 (1942)
Chen, A.L., Wood, A.C.: Rate effects on water–oil relative permeability. In: Society of Core Analysis Conference Paper (SCA 2001-19) (2001)
Christie, M.: Flow in porous media—scale up of multiphase flow. Curr. Opin. Colloid Interface Sci. **6**(3), 236–241 (2001)
Christie, M., Blunt, M.: Tenth SPE comparative solution project: a comparison of upscaling techniques. SPE Reserv. Eval. Eng. **4**(4), 308–317 (2001)
Coats, K., Dempsey, J., Henderson, J.: The use of vertical equilibrium in two-dimensional simulation of three-dimensional reservoir performance. Soc. Pet. Eng. J. **11**(1), 63–71 (1971)
Coats, K., Nielsen, R., Terhune, M.H., Weber, A.: Simulation of three-dimensional, two-phase flow in oil and gas reservoirs. Soc. Pet. Eng. J. **7**(4), 377–388 (1967)
Dale, M., Ekrann, S., Mykkeltveit, J., Virnovsky, G.: Effective relative permeabilities and capillary pressure for one-dimensional heterogeneous media. Transp. Porous Media **26**(3), 229–260 (1997)
Durlofsky, L.J.: Numerical calculation of equivalent grid block permeability tensors for heterogeneous porous media. Water Resour. Res. **27**(5), 699–708 (1991)
Durlofsky, L.J.: Upscaling of geocellular models for reservoir flow simulation: a review of recent progress. In: 7th International Forum on Reservoir Simulation, pp. 23–27 (2003)
Durlofsky, L.J.: Upscaling and gridding of fine scale geological models for flow simulation. In: 8th International Forum on Reservoir Simulation Iles Borromees, Stresa, Italy, 20–24 June 2005 (2005)
ECLIPSE 100 reservoir simulator, Schlumberger. http://www.slb.com/eclipse/
Ekrann, S., Aasen, J.O.: Steady-state upscaling. Transp. Porous Media **41**(3), 245–262 (2000)
Farmer, C.: Upscaling: a review. Int. J. Numer. Methods Fluids **40**(1–2), 63–78 (2002)
Jonoud, S., Jackson, M.D.: New criteria for the validity of steady-state upscaling. Transp. Porous Media **71**(1), 53–73 (2008)
Kjonsvik, D., Doyle, J., Jacobsen, T., et al.: The effects of sedimentary heterogeneities on production from a shallow marine reservoir—what really matters? In: SPE Annual Technical Conference and Exhibition. Society of Petroleum Engineers (1994)
Kløv, T., Øren, P., Stensen, J., Lerdahl, T., Berge, L., Bakke, S., Boassen, T., Virnovsky, G., et al.: Pore-to-field scale modeling of wag. In: SPE Annual Technical Conference and Exhibition. Society of Petroleum Engineers (2003)
Kyte, J.R., Berry, D., et al.: New pseudo functions to control numerical dispersion. Soc. Pet. Eng. J. **15**(04), 269–276 (1975)
Lake, L.W.: Enhanced Oil Recovery, reprint 2010 edn. Society of Petroleum Engineers (1989)
Lie, K.A., Krogstad, S., Ligaarden, I., Natvig, J., Nilsen, H., Skaflestad, B.: Open-source MATLAB implementation of consistent discretisations on complex grids. Comput. Geosci. **16**, 297–322 (2012)
Lohne, A., Virnovsky, G.A., Durlofsky, L.J., et al.: Two-stage upscaling of two-phase flow: from core to simulation scale. SPE J. **11**(03), 304–316 (2006)
Odsæter, L.H., Berg, C.F., Rustad, A.B.: Rate dependency in steady-state upscaling. Transp. Porous Media, 1–25 (2015)
Peaceman, D.W.: Interpretation of well-block pressures in numerical reservoir simulation with nonsquare grid blocks and anisotropic permeability. SPE J. **23**(3), 531–543 (1983)
Pickup, G., Ringrose, P., Sharif, A.: Steady-state upscaling: From lamina-scale to full-field model. SPE J. **5**(2), 208–217 (2000)
Rapoport, L.A.: Scaling laws for use in design and operation of water–oil flow models. Pet. Trans. **204**, 143–150 (1955)
Renard, P., de Marsily, G.: Calculating equivalent permeability: a review. Adv. Water Resour. **20**(5–6), 253–278 (1997)
Ringrose, P.S., Sorbie, K.S., Corbett, P.W.M., Jensen, J.L.: Immiscible flow behaviour in laminated and cross-bedded sandstones. J. Pet. Sci. Eng. **9**(2), 103–124 (1993)
Rustad, A.B., Theting, T.G., Held, R.J.: Pore space estimation, up scaling and uncertainty modeling for multiphase properties. In: SPE Symposium on Improved Oil Recovery, 20–23 April 2008, Tulsa, Oklahoma, USA (2008)
Shook, M., Li, D., Lake, L.W.: Scaling immiscible flow through permeable media by inspectional analysis. In Situ **16**(4), 311–349 (1992)
Smith, E.H.: The influence of small-scale heterogeneity on average relative permeability. In: Reservoir Characterization II, pp. 52–76. Academic Press, Inc., London (1991)
Stephen, K.D., Pickup, G.E., Sorbie, K.S.: The local analysis of changing force balances in immiscible incompressible two-phase flow. Transp. Porous Media **45**(1), 63–88 (2001)
The MATLAB Reservoir Simulation Toolbox, MRST 2015a (2015). http://www.sintef.no/MRST/

Virnovsky, G.A., Friis, H.A., Lohne, A.: A steady-state upscaling approach for immiscible two-phase flow. Transp. Porous Media **54**(2), 167–192 (2004)

Yortsos, Y.C.: A theoretical analysis of vertical flow equilibrium. Transp. Porous Media **18**(2), 107 (1995)

Zhang, P., Pickup, G.E., Christie, M.A., et al.: A new method for accurate and practical upscaling in highly heterogeneous reservoir models. In: International Oil & Gas Conference and Exhibition in China. Society of Petroleum Engineers (2006)

Zhou, D., Fayers, F., Orr Jr., F., et al.: Scaling of multiphase flow in simple heterogeneous porous media. SPE Reserv. Eng. **12**(03), 173–178 (1997)